



COMPLIMENTARY/POSTER SESSION PAPER

It Pays to Be Bumpy: Drag Reducing Armor in the Pacific Spiny Lumpsucker, *Eumicrotremus orbis*

R. C. Hoover ^{*,1}, Olivia H. Hawkins[†], Jack Rosen[‡], Conrad D. Wilson[§], Callie H. Crawford ^{*,¶}, Meghan M. Holst^{||}, Jonathan M. Huie [#], Adam P. Summers^{†,**}, Cassandra M. Donatelli^{††} and Karly E. Cohen^{††}

*Department of Biology, University of Louisiana at Lafayette, Lafayette, LA, 70503, USA; [†]Department of Biology, Tufts University, Medford, MA 02155, USA; [‡]Department of Biology, University of Washington, Seattle, WA, 98195, USA; [§]Department of Earth Sciences, Carleton University, Ottawa, ON, K1S 5B6, CA; [¶]Department of Biology, Coastal Carolina University, Conway, SC, 29528, USA; ^{||}Center for Watershed Sciences, University of California, Davis, Davis, CA, 95616, USA; [#]Department of Biological Sciences, The George Washington University, Washington, DC, 20052, USA; ^{**}Friday Harbor Laboratories, University of Washington, Friday Harbor, WA, 98250, USA; ^{††}Fowler School of Engineering, Chapman University, Orange, CA, 92866, USA; ^{††}Department of Biology, University of Florida, Gainesville, FL, 32611, USA

From the symposium “Pathways to adulthood: environmental, developmental, and evolutionary influences on the ontogeny of form and function” presented at the annual meeting of the Society for Integrative and Comparative Biology annual meeting, January 3–March 7, 2023.

¹E-mail: rchoover.research@gmail.com

Synopsis Armor is a multipurpose set of structures that has evolved independently at least 30 times in fishes. In addition to providing protection, armor can manipulate flow, increase camouflage, and be sexually dimorphic. There are potential tradeoffs in armor function: increased impact resistance may come at the cost of maneuvering ability; and ornate armor may offer visual or protective advantages, but could incur excess drag. Pacific spiny lumpsuckers (*Eumicrotremus orbis*) are covered in rows of odontic, cone-shaped armor whorls, protecting the fish from wave driven impacts and the threat of predation. We are interested in measuring the effects of lumpsucker armor on the hydrodynamic forces on the fish. Bigger lumpsuckers have larger and more complex armor, which may incur a greater hydrodynamic cost. In addition to their protective armor, lumpsuckers have evolved a ventral adhesive disc, allowing them to remain stationary in their environment. We hypothesize a tradeoff between the armor and adhesion: little fish prioritize suction, while big fish prioritize protection. Using micro-CT, we compared armor volume to disc area over lumpsucker development and built 3D models to measure changes in drag over ontogeny. We found that drag and drag coefficients decrease with greater armor coverage and vary consistently with orientation. Adhesive disc area is isometric but safety factor increases with size, allowing larger fish to remain attached in higher flows than smaller fish.

Introduction

Armor is thought to be principally for protection from, for example, piercing predators or sharp substrates (Meyers et al. 2012; Yang et al. 2013; Lowe et al. 2021; Kruppert et al. 2020). Armor has evolved at least 30 times across cartilaginous and bony fishes, and serves a wide variety of roles. These include, but are not limited to, physiological storage for calcium, sexual display, armament for combat, mechanical enhancers of stiffness, and defense (Kynard 1979; Huntingford 1982;

Rief 1985; Ruben and Bennett 1987; Bartol et al. 2005; Meyers et al. 2012; Yang et al. 2013; Lowe et al. 2021; Kruppert et al. 2020; Kolmann et al. 2020a, b; Woodruff et al. 2022). In some fishes, for example, poachers (Agonidae), there is good evidence that armor plates do serve a protective role. The function is inferred from damage—abrasive damage on the belly from substrate contact, and impact damage on the dorsum from combat or predation (Kruppert et al. 2020; Kolmann et al. 2020a). Pacific spiny lumpsuckers are covered with

Advance Access publication June 19, 2023

© The Author(s) 2023. Published by Oxford University Press on behalf of the Society for Integrative and Comparative Biology. All rights reserved. For permissions, please e-mail: journals.permissions@oup.com

whorls of lightweight, enamel armor that bears witness to impact damage (Woodruff et al. 2022). Presumably, in its defensive capacity, armor has several axes of variation that are important to performance: material properties, plate structure, and the interactions among plates (Bruet et al. 2008; Song et al. 2011; Meyes et al. 2012; Yang et al. 2013; Kruppert et al. 2020; Kolmann et al. 2020a; Lowe et al. 2021). As a first approximation, it is sensible to suppose that heavier armor, with greater coverage and plate overlap, is more protective than lighter, less overlapping armor.

It is also useful to consider the hydrodynamic impact of armor, particularly over ontogeny, because swimming speed and maneuverability are key performance traits for survival (Webb and Weihs 1986; Wassenbergh et al. 2015; Larouche et al. 2020; Sagnes et al. 2000). Bichirs (Polypteridae), gar (Lepisosteidae), and some species of poacher (Agonidae) begin life with flexible, geometrically simplified armor, which grows in density and complexity over time (Bruet et al. 2008; Song et al. 2011; Kolmann et al. 2020a). In *Polypterus*, this complexity faces inward, and increases the stiffness of the body through spines and sockets beneath the skin (Bruet et al. 2008; Song et al. 2011). Their armor, smooth throughout ontogeny, does not alter flow differentially as they get bigger. Conversely, the armor of spearnose poachers, *Agonopsis vulsa*, transitions from being porous plates with large spines in juveniles to solid scutes with small spines as adults. So, not only can armor affect flow around a fish, that effect can vary over ontogeny.

Pacific spiny lumpsuckers, *E. orbis* (Günther 1861), are small, globose, heavily armored, charismatic fish found in the rocky subtidal and submerged intertidal of the Northern Pacific Ocean (Günther 1861; Arita 1969; Kells et al. 2016; Huie et al. 2022; Woodruff et al. 2022). Their odontic armor, a lightweight derivative of teeth, is composed of small enamel cones that fuse together as the fish gets bigger (Woodruff et al. 2022). Armor changes radically over ontogeny, with large fish having more armor plates, plates with more cusps, and a greater portion of their surface covered in armor (Woodruff et al. 2022; Fig. 1). In large individuals, the armor whorls make up so much of the surface that they must affect viscous drag as water flows over the fish. It is difficult to imagine how these spiny, spherical fish could stationhold in even a light current, but they are the only armored fish with a ventral adhesive disc (Arita 1967; Budney and Hall 2010; Huie et al. 2022). The combination of potentially high drag armor and an adhesive disc makes lumpsuckers an interesting system for examining tradeoffs between different performance characteristics of armor. The scaling relationships between armor and adhesion over ontogeny should reveal the role

of the disc in resisting dislodgement due to potentially increased drag (Huie et al. 2022; Woodruff et al. 2022).

Here, we investigate the interactions between armor and hydrodynamic drag of the Pacific spiny lumpsucker over ontogeny. The objective of this study is to evaluate how changing armor over ontogeny affects drag and whether there is a relationship between the hydrodynamics of the armor and the scaling of the adhesive disc of the Pacific spiny lumpsucker. Our goals are fourfold: (1) to measure drag at several angles of attack along the horizontal plane and at several speeds, across ontogeny, using similarly sized 3D models, (2) calculate the drag over ontogeny of fish using the coefficient of drag measured from our scaled models, (3) measure adhesive disc growth over ontogeny, and (4) compare armor morphology, drag, and disc size. We predict that increased armor coverage leads to increased drag. This might be offset by increased adhesion, or perhaps the armor protects against the impacts due to dislodgement. This tradeoff would be supported by positive allometry in armor coverage, positive allometry in drag coefficient, and negative allometry of the adhesive disc, indicating a greater reliance on adhesion early in life that would be replaced over ontogeny with armor to protect them from impacts.

Materials and methods

3D segmentation and model building

We downloaded 20 micro computed tomography (micro-CT) scans of *E. orbis*, the Pacific spiny lumpsucker, used in Woodruff et al. 2022 from Morphosource.org (Boyer et al. 2016; morphosource.org, Supplementary Table S1). We also included an additional specimen ($n = 1$, at 5.4 mm standard length [SL]), captive bred and provided by M. Holst at the Aquarium of the Bay, CA, USA. This specimen was imaged at the Karel F. Liem Bio-Imaging Center at Friday Harbor Laboratories, Friday Harbor, WA, USA, with a Bruker Skyscan 1173. Scans were reconstructed in NRecon (Bruker 2005–2011) and segmented in 3D Slicer (version r29738) with the SlicerMorph extension (Kikinis et al. 2013; Rolfe et al. 2021).

We approximated the adhesive disc area using the equation for the area of an ellipse

$$\text{Area} = a * b * \pi, \quad (1)$$

where a , the major axis, is $\frac{1}{2}$ the length from the right upper internal ascending process to the lower fimbriae of the last right pelvic fin ray and b , the minor axis, is $\frac{1}{2}$ the width of the broadest point of the adhesive disc; across the distal ends of the third pelvic fin rays (Arita 1967; Budney and Hall 2010; Huie et al. 2022). We took these measurements using the markups mod-

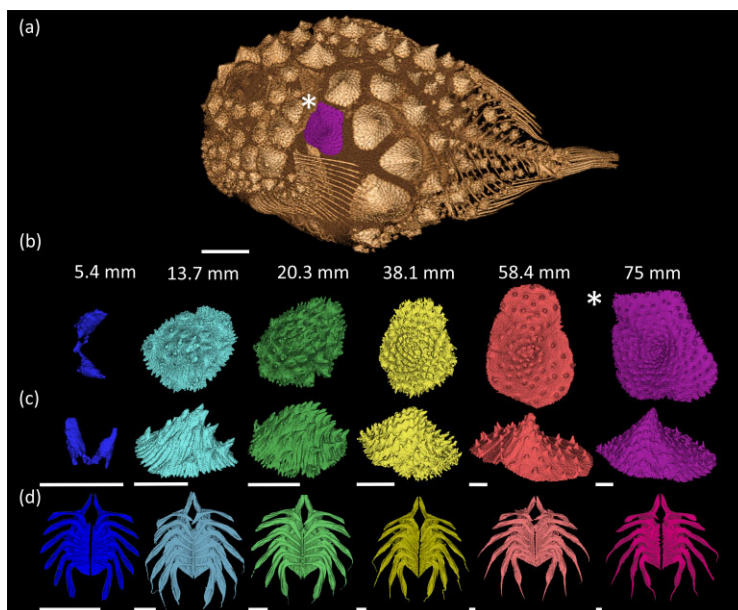


Fig. 1 CT scans of *E. orbis* odontodes and adhesive discs over ontogeny. (A) Micro-CT scan of an adult lump sucker (75 mm SL; Scale bar = 1 cm). (B) Dorsal view of representative odontodes over ontogeny showing crown development. (C) Lateral view of odontodes over development. Shape and complexity greatly increase throughout lump sucker development. All scales in panels (B) and (C) are from the same location highlighted in panel (A) (purple odontode and asterisk). The scale bar under the dark blue odontode in panels (B) and (C) is set to 0.25 mm, all other scale bars are 1.0 mm. (D) Ventral view of skeletal adhesive discs over ontogeny (Scale bar = 1 mm).

ule in 3D Slicer. We then compared our morphometric measurements to previously published data on armor volume from this series of micro-CT imaged lump suckers (Woodruff et al. 2022).

Modeling

From the 21 micro-CT scans considered for morphometrics, we selected six specimens that represented major shifts in armor morphology (Woodruff et al. 2022; Fig. 1; Table 1). Using 3D Slicer, we generated solid models by segmenting out the armor and filling the empty space between the armor and skeleton holes with iterations of the wrap solidify module, resulting in a solid body model (Weidert et al. 2020). We combined the original armor segment with the solid body using the logical operators tool (Pinter et al. 2019) to ensure that nuances in scale morphology were not hidden after wrapping. We filled any remaining voids in the model with the paintbrush tool (Pinter et al. 2019) and added a ventral support tab to each model in Blender version 3.1.2 (Blender Foundation, Amsterdam, Netherlands; blender.org.). We placed the tab on the adhesive disc on the model’s ventral side to allow flow to travel across the model as it would over a live fish adhering to the substrate. We scaled each model to 100 mm in total length (TL). Scaling by TL was used to standardize the models because the development of the tail over ontogeny is poorly described and likely does not contribute much

to drag forces. We printed models using an Ultimaker S5 3D printer (Source Graphics, Anaheim, CA, USA) with tough PLA (polylactic acid filament; 2.85 mm) and polyvinyl dissolvable supports. We used 0.4-mm nozzles printing at 55 mm s⁻¹ at fine resolution (0.2 mm), 15% infill, and 75% overhang support. We printed these models larger than life and at the fine resolution to reduce the impact of the layer lines on hydrodynamics. Odontodes are typically taller than 1mm in height on the models, an order of magnitude higher than the fine resolution layers (0.02–0.4 mm). We assigned roman numerals to the models to refer to them easily in text (Fig. 2; 5.4 mm—I, 13.7 mm—II, 20.3 mm—III, 38.1 mm—IV, 58.4 mm—V, 75.0 mm—VI) and will use this lettering hereafter.

Drag experiments

We mounted each model by its ventral support tab to a six axis force transducer; a configuration that allowed us to isolate the effects of armor separate from adhesion. We mounted the force transducer in a recirculating freshwater flume with a working area of 152.4 × 38.1 × 50.8 cm (Rolling Hills Research Corporation [RHRC] Eidetics’ Flow Visualization Water Tunnel, Model 1520; Fig. 3) and measured drag at 1.27, 2.54, and 5.08 bl s⁻¹. The force transducer rotated and recorded drag force (N) every 10° for 360° beginning with flow facing the tail (180°) and ending with flow

Table 1 3D models. Surface area and volume calculated from Blender; Reynolds numbers, based on length, calculated using reference values from Vogel (1994, 23).

| Model | Standard length (mm) | Model length (mm) | Model surface area (mm ²) | Model volume (mm ³) | Anterior 2D frontal area (mm ²) | Lateral 2D frontal area (mm ²) | Flow speed (bl s ⁻¹) | Live Re | Model Re |
|-------|----------------------|-------------------|---------------------------------------|---------------------------------|---|--|----------------------------------|----------|----------|
| I | 5.4 | 100 | 13629.49 | 65159 | 1642.2 | 3010.3 | 1.27 | 655.09 | 12649.30 |
| | | | | | | | 2.54 | 1310.19 | 25298.60 |
| | | | | | | | 5.08 | 2620.37 | 50597.21 |
| II | 13.7 | 100 | 7637.67 | 24735 | 1227.5 | 2380.3 | 1.27 | 1661.99 | 12649.30 |
| | | | | | | | 2.54 | 3323.99 | 25298.60 |
| | | | | | | | 5.08 | 6647.98 | 50597.21 |
| III | 20.3 | 100 | 13284.80 | 50684 | 1530 | 3252.7 | 1.27 | 2462.66 | 12649.30 |
| | | | | | | | 2.54 | 4925.33 | 25298.60 |
| | | | | | | | 5.08 | 9850.65 | 50597.21 |
| IV | 38.1 | 100 | 17140.82 | 76770.6 | 2116.4 | 3612.5 | 1.27 | 4622.04 | 12649.30 |
| | | | | | | | 2.54 | 9244.08 | 25298.60 |
| | | | | | | | 5.08 | 18488.17 | 50597.21 |
| V | 58.4 | 100 | 16200.82 | 84308.2 | 2523.8 | 4037.2 | 1.27 | 7084.70 | 12649.30 |
| | | | | | | | 2.54 | 14169.41 | 25298.60 |
| | | | | | | | 5.08 | 28338.82 | 50597.21 |
| VI | 75 | 100 | 14460.27 | 77384.6 | 2142.1 | 3177.8 | 1.27 | 9098.51 | 12649.30 |
| | | | | | | | 2.54 | 18197.02 | 25298.60 |
| | | | | | | | 5.08 | 36394.03 | 50597.21 |

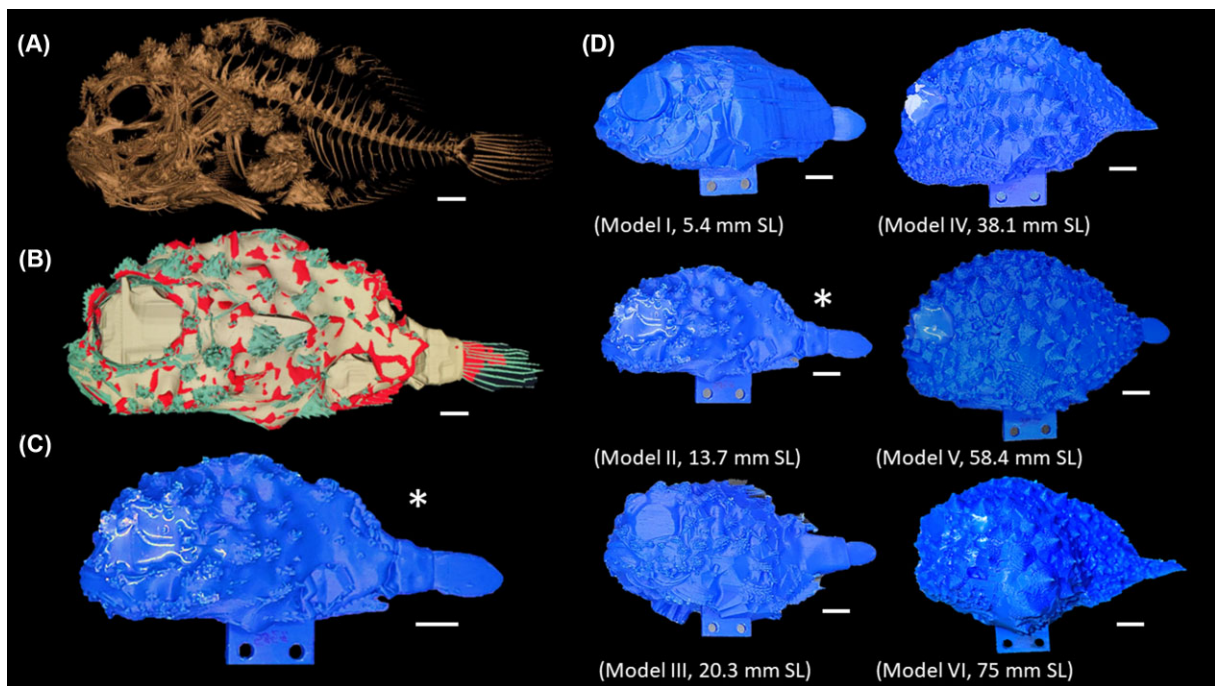


Fig. 2 Generation of 3D models. (A) Micro-CT scan of *E. orbis* (ark:/87602/m4/377572, 13.7 mm; Scale bar = 1 mm). (B) CT filled and smoothed using the wrap solidify module (Scale bar = 1 mm). (C) The resulting 3D printed model with added ventral support tab for attachment to the force transducer (Scale bar = 1 cm). (D) Ontogenic models, each model is scaled to 10 cm TL to give consistent testing conditions (Re; Scale bar = 1 cm). Asterisks denote enlarged Model II depicted in (C) and (D).

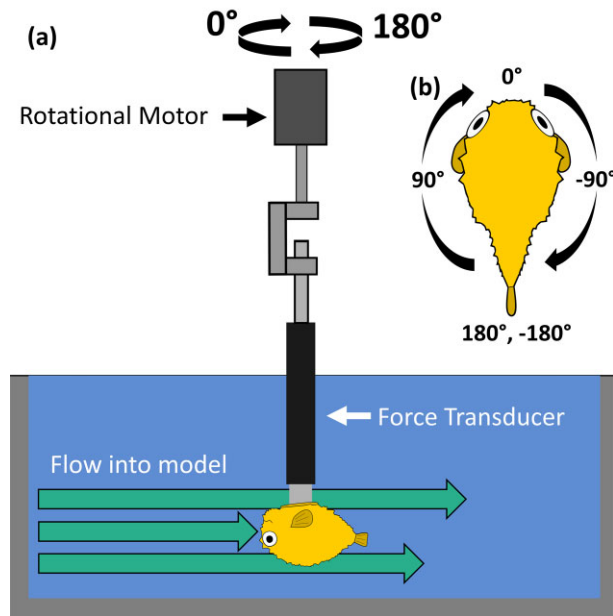


Fig. 3 Model testing in flow. (A) Schematic diagram of the Rolling Hills Research Corporation 6-axis force transducer in the fresh water flume. Models are mounted ventrally to the force transducer, which records drag force in Newtons (N) at various speeds and positions. The entire assembly rotates around its axis via the rotational motor (B), recording drag every 10° from -180° to 180°.

facing the tail (-180°). We normalized drag by volume to preserve the effect of armor coverage via surface area (Fig. 4). The anterior-posterior axis of the fish model may not have been perfectly aligned with 0° and 180° on the motor. To account for this variation, we measured local minimum for posterior and anterior measurements and measured local maximum for lateral measurements to account for small differences in orientation (Table 2).

We calculated drag coefficient using

$$C_d = \frac{2F_d}{\rho u^2 A_r}, \quad (2)$$

where C_d is the drag coefficient, F_d is the measured drag force (N), ρ is mass density (kg m^{-3}) of the fluid, u is the flow speed (m s^{-1}), and A_r is the reference area (m^2) defined by the frontal surface area from the head, side, and tail, respectively (FIJI polygon selection tool; Schindelin et al. 2012). Frontal area takes into consideration directional information about surface area and shape, as opposed to wetted surface area (Vogel 1994; Sagnes et al. 2000).

We calculated the Reynolds number (Re) using

$$Re = \frac{\rho u L}{\mu}, \quad (3)$$

where L is the length of the fish specimen (m) and μ is the dynamic viscosity of the water ($\text{m}^2 \text{s}^{-1}$; Vogel 1994).

We calculated the Re for each fish specimen and their respective models across experimental flow speeds. Values differ between freshwater (used during model testing), and saltwater (experienced by the live fish). For the density of freshwater and saltwater at 20°C, we used $0.998 \times 10^3 \text{ kg m}^{-3}$ and $1.024 \times 10^3 \text{ kg m}^{-3}$, respectively (Vogel 1994). The dynamic viscosity of freshwater (0 ppt NaCl) at 20°C is $1.002 \times 10^{-3} \text{ (Pa s)}$, and the dynamic viscosity of saltwater (35 ppt NaCl) at 20°C is $1.072 \times 10^{-3} \text{ (Pa s)}$ (Vogel 1994).

We computed drag force experienced by the fish specimens at their actual body size using

$$F_{cd} = \frac{1}{2} C_d \rho u^2 A_{rs}, \quad (4)$$

where F_{cd} is the computed drag force (N) and A_{rs} is the reference area (m^2) defined by the scaled frontal surface area (2D area measured from the models, scaled to the size of the respective fish specimen) for the anterior, posterior, and lateral sides.

We computed adhesive force using

$$F_{ca} = A_d p, \quad (5)$$

where F_{ca} is the computed adhesive force (N), A_d is the adhesive disc area, and p is the ambient pressure outside the adhesive disc, estimated at 101 kPa (Wainwright et al. 2013).

Scaling

We investigated the scaling relationships between adhesive disc area (mm^2) and armor volume (mm^3) across standard length (mm) using R version 4.1.1 (2021-08-10; R Core Team 2022). We calculated reduced major axis (RMA) regressions on \log_{10} transformed data using the *lmodel2* R package (Legendre and Okansen 2018). RMA regressions are preferred over other Model II regressions because they account for potential measurement error in both variables and are the least biased estimate of the underlying relationship (LaBarbera 1989). We compared the RMA slopes to the predicted isometric growth slopes. Scaling relationships were considered allometric if the predicted slopes for isometry were outside of the 95% confidence interval (CI) from the RMA regression slopes.

Results

Model morphology

The smallest lump sucker in our dataset (ark:/87602/m4/529160) had the least complex armor—singular cones scattered over the body with space between them. There were 24 odontodes, with a combined volume of 0.0035 mm^3 (Supplementary Table S2, Fig. 1). The odontodes were concentrated in four

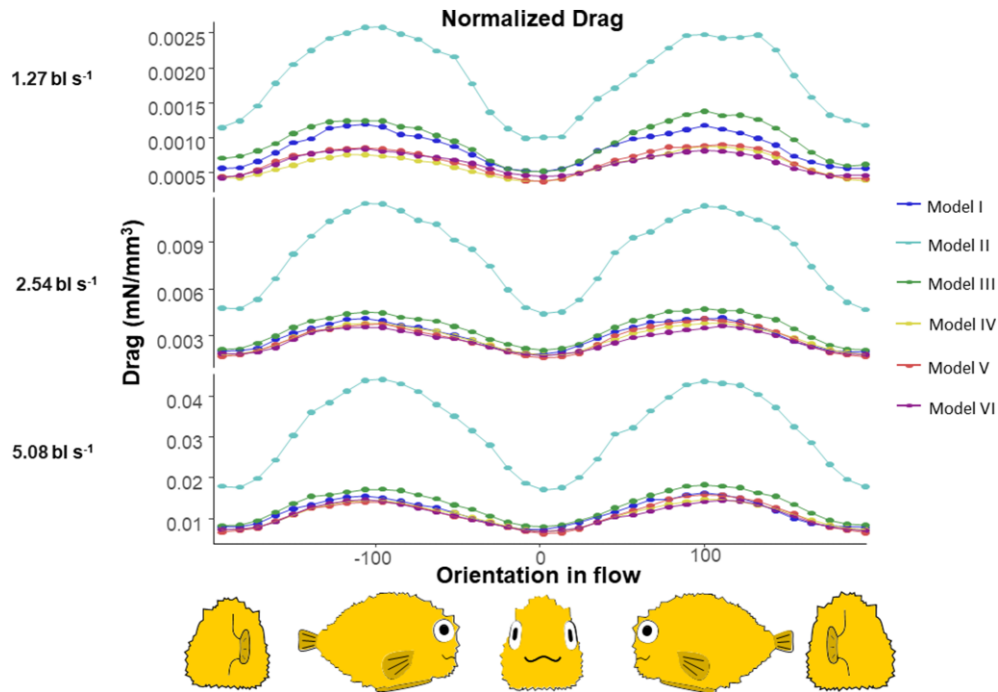


Fig. 4 Normalized drag force across model orientations and flow speeds. The flow speeds in which the models were exposed to are to the left of their respective panels. Drag varies most with orientation. The Model II (Turquoise line) has the highest drag across all flow speeds with Model III (Green) and Model I (Dark blue) with the next highest drag values.

Table 2 Drag and drag coefficients at different orientations. Drag varies most with orientation. Drag coefficients calculated from raw drag data and 2D frontal area for each orientation. Anterior (0°) of the fish had the lowest drag coefficient, then the posterior (-180° , 180°), with the lateral sides of the fish having the highest drag coefficients (-90° , 90°).

| Model | Speed (bl s^{-1}) | Drag (mN mm^{-3}) | | | | | | Drag coefficients | | | | | |
|-------|---------------------------------|------------------------------|--------|--------|--------|--------|--------|-------------------|------|------|------|------|-------|
| | | -180 | -90 | 0 | 90 | 180 | range | -180 | -90 | 0 | 90 | 180 | range |
| I | 1.27 | 0.0005 | 0.0012 | 0.0005 | 0.0011 | 0.0005 | 0.0007 | 2.62 | 3.02 | 2.4 | 3.08 | 2.64 | 0.67 |
| I | 2.54 | 0.0019 | 0.004 | 0.0017 | 0.004 | 0.0019 | 0.0023 | 2.36 | 2.57 | 2.13 | 2.67 | 2.31 | 0.53 |
| I | 5.08 | 0.0074 | 0.015 | 0.0067 | 0.0158 | 0.0073 | 0.0091 | 2.27 | 2.44 | 2.06 | 2.65 | 2.25 | 0.59 |
| II | 1.27 | 0.0011 | 0.0026 | 0.001 | 0.0024 | 0.0011 | 0.0016 | 2.8 | 3.29 | 2.44 | 3.15 | 2.87 | 0.86 |
| II | 2.54 | 0.0046 | 0.0113 | 0.0043 | 0.0111 | 0.0045 | 0.007 | 2.89 | 3.63 | 2.67 | 3.58 | 2.83 | 0.95 |
| II | 5.08 | 0.0172 | 0.0435 | 0.0165 | 0.043 | 0.0173 | 0.027 | 2.71 | 3.5 | 2.58 | 3.46 | 2.7 | 0.92 |
| III | 1.27 | 0.0007 | 0.0012 | 0.0005 | 0.0014 | 0.0006 | 0.0009 | 2.79 | 2.34 | 2.03 | 2.61 | 2.43 | 0.76 |
| III | 2.54 | 0.002 | 0.0044 | 0.0019 | 0.0046 | 0.002 | 0.0026 | 2.05 | 2.09 | 2 | 2.21 | 2.02 | 0.21 |
| III | 5.08 | 0.0077 | 0.0167 | 0.0075 | 0.0177 | 0.0079 | 0.0103 | 1.99 | 2.01 | 1.91 | 2.14 | 2.02 | 0.23 |
| IV | 1.27 | 0.0004 | 0.0007 | 0.0004 | 0.0008 | 0.0004 | 0.0005 | 1.86 | 1.86 | 1.6 | 2.21 | 1.64 | 0.61 |
| IV | 2.54 | 0.0017 | 0.0037 | 0.0017 | 0.0037 | 0.0017 | 0.002 | 1.9 | 2.43 | 1.88 | 2.43 | 1.91 | 0.56 |
| IV | 5.08 | 0.0068 | 0.014 | 0.0063 | 0.0142 | 0.0068 | 0.0079 | 1.91 | 2.31 | 1.78 | 2.34 | 1.91 | 0.56 |
| V | 1.27 | 0.0004 | 0.0008 | 0.0003 | 0.0009 | 0.0004 | 0.0005 | 1.7 | 2.1 | 1.43 | 2.23 | 1.6 | 0.8 |
| V | 2.54 | 0.0016 | 0.0037 | 0.0015 | 0.0039 | 0.0016 | 0.0025 | 1.64 | 2.37 | 1.54 | 2.55 | 1.61 | 1.02 |
| V | 5.08 | 0.0061 | 0.0136 | 0.0058 | 0.0154 | 0.006 | 0.0096 | 1.58 | 2.19 | 1.49 | 2.48 | 1.56 | 1 |
| VI | 1.27 | 0.0004 | 0.0008 | 0.0004 | 0.0008 | 0.0004 | 0.0004 | 1.79 | 2.34 | 1.86 | 2.38 | 1.94 | 0.59 |
| VI | 2.54 | 0.0017 | 0.0034 | 0.0016 | 0.0035 | 0.0017 | 0.0019 | 1.97 | 2.58 | 1.79 | 2.55 | 1.89 | 0.79 |
| VI | 5.08 | 0.0068 | 0.0141 | 0.0064 | 0.014 | 0.0066 | 0.0078 | 1.92 | 2.59 | 1.79 | 2.57 | 1.85 | 0.81 |

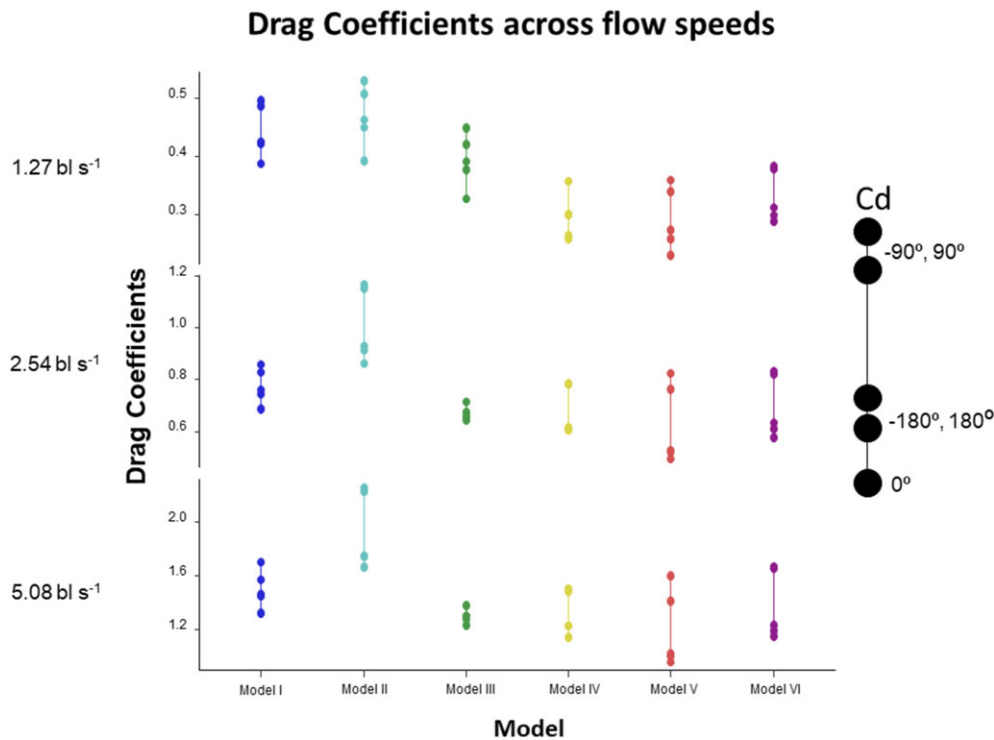


Fig. 5 Drag coefficients across flow speeds. Drag coefficients calculated from raw drag data and 2D frontal area for each orientation, represented by the legend on the right. Anterior (0°) of the fish had the lowest drag coefficient, then the posterior ($-180^\circ, 180^\circ$), with the lateral sides of the fish having the highest drag coefficients ($-90^\circ, 90^\circ$; Table 2). Model II (Turquoise) has the highest drag coefficients across flow speeds.

areas: the dorsum of the head, the base of the dorsal fin, above the pectoral fins, and at the widest point of the abdomen. These odontodes were only single-cusped cones and did not resemble the highly topographic cones observed in bigger fish.

The segmented models allowed us to quantify surface area, volume, and armor morphology over ontogeny (Table 1 and Supplementary Table S2). Model I was smooth, with very little armor. Model IV had ≈ 6 times the armor of Model II and ≈ 4.5 times the armor volume of Model III. Models V and VI were completely covered in armor, while the other models had unprotected areas. Model VI had ≈ 17 times the armor than IV, and ≈ 3 times the armor of Model V. Increases in armor volume and coverage decreased surface area to volume ratio. Model II with widely spaced, rugose armor had the highest surface area to volume ratio at 3.08. Model III had a lower surface area to volume ratio at 2.62. The most heavily armored lump sucker had a surface area to volume ratio of 1.87, $\approx 60\%$ of Model II.

Across ontogeny, lump suckers experience a wide range in Re , spanning the transitional range (≈ 100 to $\approx 10,000$). The length of the specimens, combined with our experimental flow speeds gave a Re between 655 and 36,394 (Table 1). The largest specimens would

experience flow dominated almost entirely by inertial forces. In contrast, our models operated from the low end of the inertial flow regime and up, so the forces were functionally exclusively inertial (12,649–50,597; Table 1).

Drag, drag coefficient, computed drag, and computed adhesion

Normalized drag (F_n) varied in magnitude across all models and flow speeds, with the larger lump suckers (Models IV, V, and VI) experiencing less F_n than the smaller lump suckers (Models I, II, and III). The second smallest lump sucker (Model II) experienced about three times the amount of F_n as the largest lump suckers (Figs. 3 and 4; Table 2). F_n varied most with model orientation and was consistently lower when the anterior of the fish model (0°) was toward oncoming flow. F_n was slightly higher for all models when the posterior of the fish model ($180, -180^\circ$) was facing the oncoming flow (Fig. 3; Table 2). The lateral faces of all models ($90^\circ, -90^\circ$) experienced on average 2.4 times the amount of F_n than any other surface. This was expected as the lateral face of the fish model also represents the largest projected area into the flow.

Drag coefficients (C_d) followed a similar pattern to the measured drag force, but with variation across model orientation. Larger lumpsuckers (Models IV, V, and VI) had lower C_d than smaller lumpsuckers (Models I, II, and III; Fig. 5; Table 2). C_d varied consistently with orientation; anteriorly facing models (0°) had the lowest C_d , posteriorly facing models (180° , -180°) had slightly higher C_d , and models perpendicular to the flow (90° , -90°) had coefficients that were on average 1.33 times greater than anteriorly facing models (Table 2). Across the anterior (0°) and posterior (180° , -180°) model faces and at each flow speed (1.27, 2.54, 5.08 bl s^{-1}), Model V had the lowest C_d , followed by Model IV, Model VI, Model III, Model I, then Model II. This corresponded with changes in armor morphology and coverage, with larger lumpsuckers possessing armor that approximates single-cusped cones, and smaller lumpsuckers possessing widely spaced aggregations of cones on their armor, particularly Models II and III (Figs. 1 and 2). The lateral sides of the model had a slightly different trend across flow speeds. At slow speeds (1.27 bl s^{-1}), Model IV had the lowest C_d , followed by Model V, Model VI, Model III, Model I, then Model II. But at medium (2.54 bl s^{-1}) and high flow speeds (5.08 bl s^{-1}), Model III had the lowest C_d , followed by Model IV, Model V, Model VI or Model I, then Model II.

Computed drag (F_{cd}) increased with body size and flow speed (Fig. 6; Table 3). The smallest lump-sucker experienced 23.7 mN of force, while Model II at twice the length experienced an ≈ 2 -fold increase in F_{cd} . The largest lumpsucker, which is ≈ 14 times longer than the smallest, experienced a ≈ 16 -fold increase in F_{cd} . Computed drag increases by ≈ 2 -fold when the orientation of the model is lateral to the flow, except for Model II, which was closer to three-fold.

Computed adhesive force (F_{ca}) increased by over 100-fold across our size range (Supplementary Table S2, Figs. 7 and 8). Safety factor, the ratio between computed adhesion and computed drag, was lower in the smaller lumpsuckers (Models I, II, and III), and higher in the larger lumpsuckers (Models IV, V, and VI). The smallest lumpsucker had a safety factor less than two for all orientations, while Models II and III had similar safety factors, between 2 and 6. Model IV had safety factors between 3 and 8, while Model V and Model VI had safety factors between 6 and 16.

Allometry of armor and adhesive disc

Large lumpsuckers (>30 mm SL) had proportionally more armor than smaller lumpsuckers, but similarly sized discs ($r^2 = 0.93$; Fig. 7). We found positive al-

lometric growth of armor volume over ontogeny (isometric slope = 3, actual slope = 3.82, 95% CI = 3.38, 4.32, $r^2 = 0.94$). Adhesive disc area was isometric (isometric slope = 2, actual slope = 1.90, 95% CI = 1.84, 2.00, $r^2 = 0.99$) and armor volume over disc area was positively allometric (isometric slope = 1.5, actual slope = 2.01, 95% CI = 1.76, 2.29, $r^2 = 0.99$).

Discussion

For Pacific spiny lumpsuckers, it pays to be bumpy. As we predicted, bigger lumpsuckers have greater total drag (F_{cd}) but importantly, a lower than expected drag coefficient (C_d). This means that larger lumpsuckers, completely covered in complex armor, experience proportionally less normalized drag (F_n) than smaller, less well armored fish (Figs. 4, 5, 6, and 8). We propose normalized drag (F_n) and drag coefficients (C_d) increase from the smallest to the next smallest fish because the widely spaced armor plates transition from smooth to highly rugose, widely spaced structures that stick out quite far from the surface. As the fish grows beyond this high normalized drag (F_n) size, the armor becomes more closely spaced and regular, and the normalized drag (F_n) decreases because these bumps serve to increase the attached flow, much as the dimpling in a golf ball decreases drag. The relative decrease in surface area from aggregate spines to cones should also decrease friction (viscous drag) of the water over the surface of the fish (Vogel 1994; Fletcher et al. 2014; Kruppert et al. 2020; Kolmann et al. 2020a).

Armor serves different functions over ontogeny (Kruppert et al. 2020; Kolmann et al. 2020a; Eigen et al. 2022). Increased normalized drag (F_n) on smaller fish may simply be the cost of growing complex armor, or proportionally large spines may protect small lumpsuckers from predation by increasing the gape necessary to consume them (Kolmann et al. 2020a; Woodruff et al. 2022). Pea sized lumpsuckers may also use increased normalized drag (F_n) to their advantage. The smallest lumpsuckers live in the transitional regime ($1 < Re < 1000$, Table 1) and may use their armor to slow sinking in the water column. Northern spearnose poachers, *Agonopsis vulsa*, are another heavily armored fish native to the Northern Pacific ocean. Both poachers and Pacific spiny lumpsuckers lack swimbladders and cannot regulate their buoyancy internally (Budney and Hall 2010; Kolmann et al. 2020a). Juvenile poachers spend more time feeding in the water column and have proportionally longer spines on their armor than the benthic adults (Kolmann et al. 2020a). Juvenile armor morphology in both groups may increase viscous drag and facilitate feeding in the water column, a niche

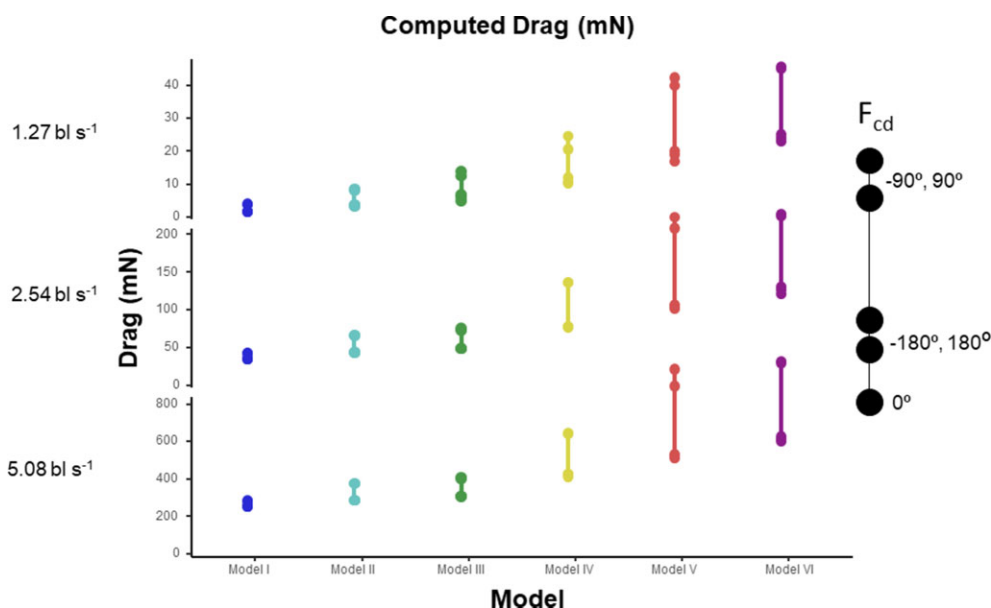


Fig. 6 Computed drag across flow speeds. Computed drag calculated from drag coefficients and scaled 2D frontal area for each orientation, represented by the legend on the right. Frontal area measured from 3D models, then scaled to the size of the live fish. Drag increases with body size.

Table 3 Computed drag at different orientations. Computed drag calculated from drag coefficients and scaled 2D frontal area for each orientation. Frontal area measured from 3D models, then scaled to the size of the live fish. Drag increases with body size.

| Model | Speed (bl s ⁻¹) | -180 | -90 | 0 | 90 | 180 | Range |
|-------|-----------------------------|--------|--------|--------|--------|--------|--------|
| I | 1.27 | 1.89 | 3.99 | 1.73 | 4.07 | 1.9 | 1.73 |
| I | 2.54 | 6.8 | 13.6 | 6.15 | 14.08 | 6.65 | 6.15 |
| I | 5.08 | 26.13 | 51.54 | 23.69 | 55.9 | 25.89 | 23.69 |
| II | 1.27 | 3.79 | 8.65 | 3.3 | 8.29 | 3.89 | 3.3 |
| II | 2.54 | 15.66 | 38.15 | 14.5 | 37.66 | 15.36 | 14.5 |
| II | 5.08 | 58.87 | 147.48 | 56.07 | 145.65 | 58.69 | 56.07 |
| III | 1.27 | 6.98 | 12.46 | 5.08 | 13.91 | 6.08 | 5.08 |
| III | 2.54 | 20.5 | 44.52 | 20.05 | 47.14 | 20.23 | 20.05 |
| III | 5.08 | 79.55 | 171.57 | 76.66 | 182.4 | 80.91 | 76.66 |
| IV | 1.27 | 12.08 | 20.68 | 10.42 | 24.57 | 10.66 | 10.42 |
| IV | 2.54 | 49.49 | 107.96 | 48.81 | 107.79 | 49.66 | 48.81 |
| IV | 5.08 | 198.29 | 410.13 | 184.73 | 415.22 | 198.29 | 184.73 |
| V | 1.27 | 20.16 | 40.01 | 16.94 | 42.34 | 19.02 | 16.94 |
| V | 2.54 | 77.93 | 180.02 | 73 | 194.31 | 76.63 | 73 |
| V | 5.08 | 301.34 | 667.62 | 283.16 | 755.95 | 296.14 | 283.16 |
| VI | 1.27 | 23.15 | 45.04 | 24.05 | 45.71 | 25.12 | 23.15 |
| VI | 2.54 | 102.09 | 198.5 | 92.75 | 195.83 | 98.08 | 92.75 |
| VI | 5.08 | 397.01 | 797.34 | 370.31 | 790.67 | 383.66 | 370.31 |

lost with growth and size (Kolmann et al. 2020a; Figs. 1, 2, and 4).

Adhesion in fish has evolved at least eight times and typically larger discs produce more adhesive force, scaling with disc area (Wainwright et al. 2013; Maie and Blob 2021; Huie et al. 2022). We hypothesized that for small fish living in a viscous, low *Re* environment, ad-

hesion would provide an avenue of protection separate from armor, and these smaller fish would have proportionately larger discs. Bigger fish living in a high *Re* environment do not face the same types of hydrodynamic forces (Alexander 1968; Vogel 1994; McHenry and Lauder 2006). Therefore, we expected that as armor coverage increases, the disc would be less im-

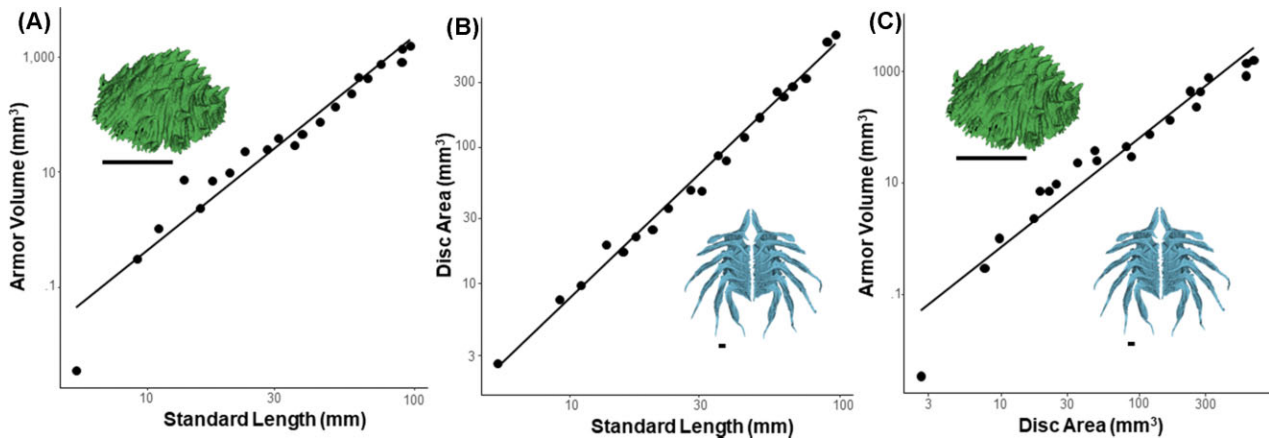


Fig. 7 Allometry of armor and suction disc over ontogeny via reduced major axis (RMA) regressions. (A) Positive allometric growth of armor volume over ontogeny (Isometric slope = 3, actual slope = 3.82, 95% CI = 3.38, 4.32, $r^2 = 0.939$). (B) Isometric growth in suction disc over ontogeny (Isometric slope = 2, actual slope = 1.90, 95% CI = 1.84, 2.00, $r^2 = 0.991$). (C) Disc area against armor volume (Isometric slope = 1.5, actual slope = 2.01, 95% CI = 1.76, 2.29, $r^2 = 0.991$). Axes are log scaled. (Scale bars = 1 mm)

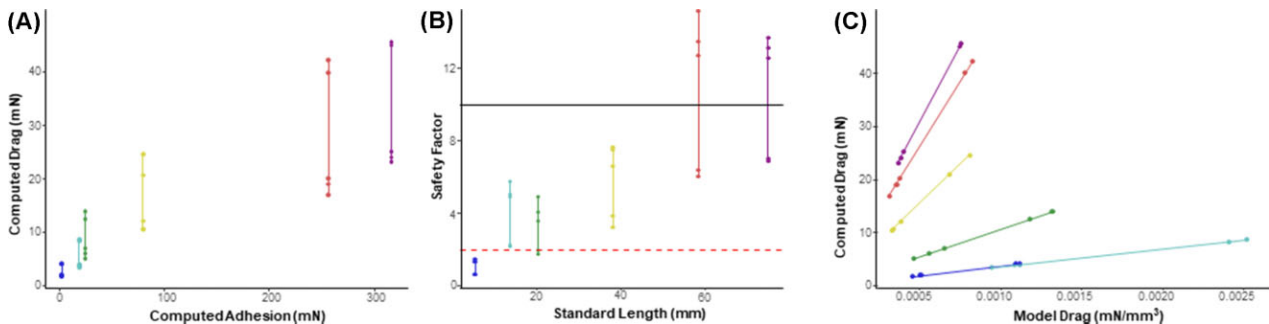


Fig. 8 Computed drag compared to computed adhesion and model drag. (A) Computed total drag at 1.27 bl s^{-1} by computed adhesion for live lumpstickers. Computed adhesion is estimated from adhesive disc area. Computed drag does not scale linearly with computed adhesion. (B) Safety factor calculated as the ratio between computed adhesion and computed drag. The red dashed line indicates a safety factor of 2, and the black line indicates a safety factor of 10. Safety factor increases with body size. (C) Computed drag by model drag, normalized by volume. Larger fish experience higher total drag forces, but smaller amounts of drag per unit volume, and less proportional change in drag based on orientation.

portant, and thus proportionately smaller. Instead, we found the disc grows isometrically, as does adhesion (Fig. 7). Coupled with the decreasing relative computed drag (F_{cd}), this leads to an increasing safety factor as the fish grows (Fig. 8). In other words, larger fish can remain attached in higher flows than can smaller fish. It is hypothesized that safety factor increases in response to unpredictable forces in limpets, seaweed, and barnacles (Murdock and Currey 1978; Alexander 1981; Lowell 1985; Koehl 1999). In waterfall-climbing gobies, safety factor increases over ontogeny (Maie and Blob 2021), potentially due to post-recruitment movement and migration through high flow waterfalls and seasonal flooding. There is a lack of literature on the ecology and behaviors of Pacific spiny lumpstickers, so we must rely on field observations and what we know mechanistically to make predictions about their ecology. Momentum increases with mass, and larger lump-

suckers sustain damage to their armor from impacts (Woodruff et al. 2022), so a higher safety factor may mitigate the number of impacts endured in adulthood. Lumpsticker adults are also globose, while smaller fish are better able to hide from flow in the complex intertidal, sitting between rocks, shielded from wave action.

Funding

This work was supported by Emily Kane, University of Louisiana at Lafayette Start-up funding [to R.C.H., O.H.H., and C.H.C.]; the Stephen and Ruth Wainwright Fellowship at Friday Harbor Laboratories (FHL) [to R.C.H., O.H.H., C.D.W., J.M.H., and K.E.C.], Adopt-a-student program at FHL [to R.C.H. and C.D.W.]; NSERC Alexander Graham Bell Canada Graduate Scholarship [to C.D.W.]; NSERC Systematics Supplement provided by the Canadian Museum of Na-

ture [to C.D.W.]; Tetsuto Miyashita NSERC Discovery Grant [to C.D.W.]; the Company of Biologists Traveling Fellowship (JEB) [to C.H.C.]; Ellen Coussan Endowed Biology Student Scholarship at the University of Louisiana at Lafayette [to O.H.H.]; Aquarium of the Bay in San Francisco, CA, USA [to M.M.H.]; Chapman University Start-up funds [to C.M.D.]; National Science Foundation [DBI-1759637 and DBI-1852096 to A.P.S.]; National Science Foundation Graduate Research fellowship [DGE-1746914 to J.M.H.].

Acknowledgments

We give special thanks to Katherine Maslenikov, the ichthyology collections manager at the Burke museum, for access to specimens; the Karel F. Liem Bioimaging center for access to CT scanning and reconstructing equipment.

Supplementary data

Supplementary data available at [ICB](#) online.

Conflict of Interest Statement

The authors declare no competing or financial interests.

Data availability

All CT scans and data are uploaded and freely available for download at www.morphosource.org.

References

- Alexander RM. 1968. Animal mechanics. 1st ed. London: Sidgwick & Jackson.
- Alexander RM. 1981. Factors of safety in the structure of animals. *Sci Prog Oxf* 67:109–30.
- Arita GS. 1967. A comparative study of the structure and function of the adhesive apparatus of the Cyclopteridae and Gobiesocidae [dissertation]. University of British Columbia. Vancouver
- Arita GS. 1969. Sexual dimorphism in the cyclopterid fish *Eumicrotremus orbis*. *J Fish Res Bd Can* 26:3262–5.
- Bartol IK, Gharib M, Webb PW, Weihs D, Gordon MS. 2005. Body-induced vortical flows: a common mechanism for self-corrective trimming control in boxfishes. *J Exp Biol* 208:327–44.
- Boyer DM, Gunnell GF, Kaufman S, McGeary TM. 2016. Morphosource: archiving and sharing 3-D digital specimen data. *Paleontol Soc Pap* 22:157–81.
- Bruet BJ, Song J, Boyce MC, Ortiz C. 2008. Materials design principles of ancient fish armour. *Nature Mater* 7:748–56.
- Budney LA, Hall BK. 2010. Comparative morphology and osteology of pelvic fin-derived midline suckers in lumpfishes, snailfishes and gobies. *J Appl Ichthyol* 26:167–75.
- Eigen L, Baum D, Dean MN, Werner D, Wölfer J, Nyakatura JA. 2022 Ontogeny of a tessellated surface: carapace growth of the longhorn cowfish *Lactoria cornuta*. *J Anat* 241:565–80.
- Fletcher T, Altringham J, Peakall J, Wignall P, Dorrell R. 2014. Hydrodynamics of fossil fishes. *Proc R Soc B* 281:20140703.
- Günther A. 1861. Catalogue of the acanthopterygian fishes in the collection of the British Museum. Gobiidae, Discoboli, Pediculi, Blenniidae, Labyrinthici, Mugilidae, Notacanthi. Vol. 3. London. p. British Museum (Natural History) 1–586.
- Huie JM, Wainwright DK, Summers AP, Cohen KE. 2022. Sticky, stickier and stickiest—a comparison of adhesive performance in clingfish, lump suckers and snailfish. *J Exp Biol* 225:jeb244821.
- Huntingford FA. 1982. Do inter- and intraspecific aggression vary in relation to predation pressure in sticklebacks? *Anim Behav* 30:909–16.
- Kells VA, Rocha LA, Allen LG. 2016. A field guide to coastal fishes: from Alaska to California. Baltimore, MD: Johns Hopkins University Press.
- Kikinis R, Pieper SD, Vosburgh KG. 2013. 3D Slicer: a platform for subject-specific image analysis, visualization, and clinical support. In: Jolesz F, editor. Intraoperative imaging and image-guided therapy. New York, NY: Springer New York. p. 277–89.
- Koehl MA. 1999. Ecological biomechanics of benthic organisms: life history, mechanical design and temporal patterns of mechanical stress. *J Exp Biol* 202:3469–76.
- Kolmann MA, Peixoto T, Pfeiffenberger JA, Summers AP, Donatelli CM. 2020a. Swimming and defence: competing needs across ontogeny in armoured fishes (Agonidae). *J R Soc Interface* 17:20200301.
- Kolmann MA, Urban P, Summers AP. 2020b. Structure and function of the armored keel in piranhas, pacus, and their allies. *Anat Rec* 303:30–43.
- Kruppert S, Chu F, Stewart MC, Schmitz L, Summers AP. 2020. Ontogeny and potential function of poacher armor (Actinopterygii: agonidae). *J Morphol* 281:1018–28.
- Kynard BE. 1979. Nest habitat preference of low plate number morphs in threespine sticklebacks (*Gasterosteus aculeatus*). *Copeia* 1979:525–8.
- LaBarbera M. 1989. Analyzing body size as a factor in ecology and evolution. *Annu Rev Ecol Syst* 20:97–117.
- Larouche O, Benton B, Corn KA, Friedman ST, Gross D, Iwan M, Price SA. 2020. Reef-associated fishes have more maneuverable body shapes at a macroevolutionary scale. *Coral Reefs* 39:1427–39.
- Legendre P, Oksanen MJ. 2018. Package “lmodel2”. R-project.org/package = lmodel2. <https://CRAN>. last accessed 01/15/2023.
- Lowe A, Summers AP, Walter RP, Walker S, Paig-Tran EM. 2021. Scale performance and composition in a small Amazonian armored catfish, *Corydoras trilineatus*. *Acta Biomater* 121:359–70.
- Lowell RB. 1985. Selection for increased safety factors of biological structures as environmental unpredictability increases. *Science* 228:1009–11.
- Maie T, Blob RW. 2021. Adhesive force and endurance of the pelvic sucker across different modes of waterfall-climbing in gobiid fishes: contrasting climbing mechanisms share aspects of ontogenetic change. *Zoology* 149:125969.
- McHenry MJ, Lauder GV. 2006. Ontogeny of form and function: locomotor morphology and drag in zebrafish (*Danio rerio*). *J Morphol* 267:1099–109.

- Meyers MA, Lin YS, Olevsky EA, Chen PY. 2012. Battle in the Amazon: arapaima versus piranha. *Adv Eng Mater* 14:B279–88.
- Murdock GR, Currey JD. 1978. Strength and design of shells of the two ecologically distinct barnacles, *Balanus balanus* and *Semibalanus (Balanus) Balanoides* (Cirripedia). *Biol Bull* 155:169–92.
- Pinter C, Lasso A, Fichtinger G. 2019. Polymorph segmentation representation for medical image computing. *Comput Methods Programs Biomed* 171:19–26.
- R Core Team. 2022. R: A language and environment for statistical computing. Vienna, Austria: R Foundation for Statistical Computing. <https://www.R-project.org/>. last accessed 03/15/2023.
- Reif WE. 1985. Squamation and ecology of sharks. Senckenbergische Naturforschende Gesellschaft.
- Rolfe S, Pieper S, Porto A, Diamond K, Winchester J, Shan S, Kirveslahti H, Boyer D, Summers A, Maga AM. 2021. SlicerMorph: an open and extensible platform to retrieve, visualize and analyze 3D morphology. *Methods Ecol Evol* 12:1816–25.
- Ruben JA, Bennett AA. 1987. The evolution of bone. *Evolution* 41:1187–97.
- Sagnes P, Champagne J-Y, Morel R. 2000. Shifts in drag and swimming potential during grayling ontogenesis: relations with habitat use. *J Fish Biol* 57:52–68.
- Schindelin J, Arganda-Carreras I, Frise E, Kaynig V, Longair M, Pietzsch T, Cardona A. 2012. Fiji: an open-source platform for biological-image analysis. *Nat Methods* 9:676–82.
- Song J, Ortiz C, Boyce MC. 2011. Threat-protection mechanics of an armored fish. *J Mech Behav Biomed Mater* 4:699–712.
- Van Wassenbergh S, van Manen K, Marcroft TA, Alfaro ME, Stamhuis EJ. 2015. Boxfish swimming paradox resolved: forces by the flow of water around the body promote manoeuvrability. *J R Soc Interface* 12:20141146.
- Vogel S. 1994. *Life in moving fluids*. 2nd ed. Princeton, NJ: Princeton University.
- Wainwright DK, Kleinteich T, Kleinteich A, Gorb SN, Summers AP. 2013. Stick tight: suction adhesion on irregular surfaces in the northern clingfish. *Biol Lett* 9:20130234.
- Webb PW, Weihs D. 1986. Functional locomotor morphology of early life history stages of fishes. *Trans Am Fish Soc* 115:115–27.
- Weidert S, Andress S, Linhart C, Suero EM, Greiner A, Böcker W, Kammerlander C, Becker CA. 2020. 3D printing method for next-day acetabular fracture surgery using a surface filtering pipeline: feasibility and 1-year clinical results. *Int J CARS* 15:565–75.
- Woodruff EC, Huie JM, Summers AP, Cohen KE. 2022. Pacific spiny lump sucker armor—development, damage, and defense in the intertidal. *J Morphol* 283: 164–73.
- Yang W, Gludovatz B, Zimmermann EA, Bale HA, Ritchie RO, Meyers MA. 2013. Structure and fracture resistance of alligator gar (*Atractosteus spatula*) armored fish scales. *Acta Biomater* 9:5876–89.